energies

Article

Investigation of Laminar–Turbulent Transition on a Rotating Wind-Turbine Blade of Multimegawatt Class with Thermography and Microphone Array

Torben Reichstein [1,†], Alois Peter Schaffarczyk [1,*,†], Christoph Dollinger [2,†], Nicolas Balaresque [3,†], Erich Schülein [4,†], Clemens Jauch [5,†] and Andreas Fischer [2,†]

[1] Kiel University of Applied Sciences, Grenzstrasse 3, D-24149 Kiel, Germany; torben.reichstein@gmx.de
[2] Bremen Institute for Metrology, Automation and Quality Science, University of Bremen, D-28359 Bremen, Germany; dollinger@uni-bremen.de (C.D.); andreas.fischer@bimaq.de (A.F.)
[3] Deutsche WindGuard Engineering GmbH, D-27580 Bremerhaven, Germany; n.balaresque@windguard.de
[4] DLR, German Aerospace Center, Institute of Aerodynamics and Flow Technology, D-37073 Göttingen, Germany; erich.schuelein@dlr.de
[5] Flensburg University of Applied Sciences, Kanzleistrass 91-93, D-24943 Flensburg, Germany; Clemens.Jauch@HS-Flensburg.de
* Correspondence: Alois.Schaffarczyk@FH-Kiel.de
† These authors contributed equally to this work.

Received: 18 April 2019; Accepted: 23 May 2019; Published: 1 June 2019

Abstract: Knowledge about laminar–turbulent transition on operating multi megawatt wind turbine (WT) blades needs sophisticated equipment like hot films or microphone arrays. Contrarily, thermographic pictures can easily be taken from the ground, and temperature differences indicate different states of the boundary layer. Accuracy, however, is still an open question, so that an aerodynamic glove, known from experimental research on airplanes, was used to classify the boundary-layer state of a 2 megawatt WT blade operating in the northern part of Schleswig-Holstein, Germany. State-of-the-art equipment for measuring static surface pressure was used for monitoring lift distribution. To distinguish the laminar and turbulent parts of the boundary layer (suction side only), 48 microphones were applied together with ground-based thermographic cameras from two teams. Additionally, an optical camera mounted on the hub was used to survey vibrations. During start-up (SU) (from 0 to 9 rpm), extended but irregularly shaped regions of a laminar-boundary layer were observed that had the same extension measured both with microphones and thermography. When an approximately constant rotor rotation (9 rpm corresponding to approximately 6 m/s wind speed) was achieved, flow transition was visible at the expected position of 40% chord length on the rotor blade, which was fouled with dense turbulent wedges, and an almost complete turbulent state on the glove was detected. In all observations, quantitative determination of flow-transition positions from thermography and microphones agreed well within their accuracy of less than 1%.

Keywords: boundary-layer transition; wind turbine; thermography; aerodynamic glove

---

1. Introduction

Wind energy [1] has been very successful over the past few years, with more than 50 GW newly added rated wind power each year. One important part in any design of wind turbines (WTs), especially for WT blades, is aerodynamics [2]. This consists of defining chord, twist, and appropriate 2D airfoil sections. From inviscid fluid mechanics, it is well known that design rules, if formulated in terms of circulation, only give expressions for $c \cdot c_L$ (chord times the lift coefficient) [2]. As so-called profile losses can be estimated by 1.5 tip-speed-ratio/lift-to-drag [2], those with low drag are particularly interesting. From airplanes, laminar airfoils [3] are known and widely used to reduce fuel consumption during cruise flight, and it is tempting to use this kind of airfoil for WTs, as well. A so-called operating or design point ($\alpha_{des}, c_{L,des}$) was found by constructing a tangent from the origin of the coordinate system to the $c_L(c_D)$ curve to reach for maximum lift over drag ($c_L/c_D =$ L2D), (see Figure 1). Data calculated by Xfoil for the aerofoil profile are shown in Figure 1 and summarized in Table 1.

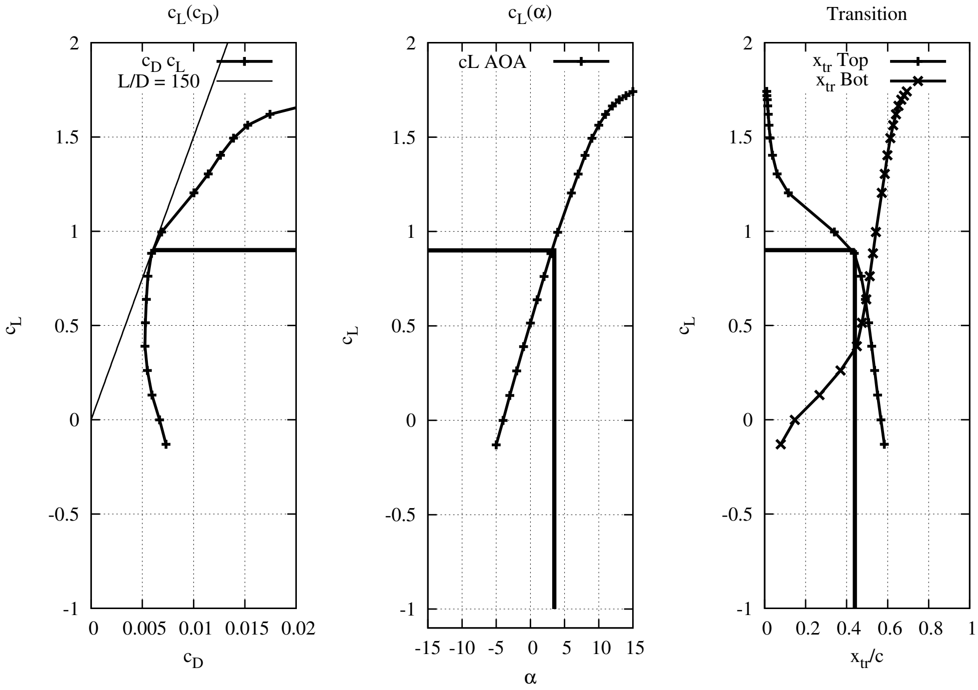

Figure 1. Determination of operating point for aerodynamic profile. See Table 1 for numbers and Figure 2 for an outline of the shape.

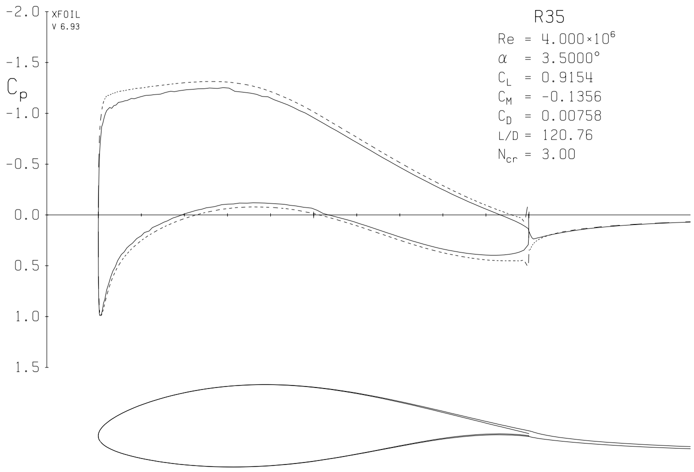

Figure 2. Static pressure on profile from Figure 1 using Xfoil. Angle of attack (AOA) is 3.5°.

Table 1. Assumed operation point for profile at R = 35, from Xfoil simulation.

Quantity	Value	Unit
$c_{L,des}$	0.9	-
$c_{D,min}$	0.005	-
Maximum lift over drag (L2D)	150	-
Angle of attack	3.5	deg
Laminar part (suction or top side)	0.45	x/c

The airfoil profile can be found at a radius of R = 35 m on the investigated WT rotor. Usually, a newly designed airfoil has to be tested in a wind tunnel. See [4] for an impressive example of high Reynolds number wind-tunnel testing, and a comparison with computational fluid dynamics (CFD). Panel codes like Xfoil, as well as genuine CFD codes like DLR-TAU [5], were used. Here, Reynolds number and inflow-turbulence levels were varied, and both effects could be simulated well. Furthermore, measured results agreed up to few percent in the lift-to-drag ratio.

As for an airplane, and much more pronounced for WTs, ambient conditions may substantially differ, especially with regard to inflow turbulence from wind-tunnel settings. Therefore, field tests are more or less inevitable. In fact, one of the authors of this paper was inspired by [6] for a comparable experiment on WT blades. In [7], a state-of-the-art version of an aerodynamic glove used on a small airplane is described. Unfortunately, this state of sophistication in measurement equipment has not yet been reached for WT blades.

First, an investigation with emphasis on the laminar–turbulent transition in the boundary layer was reported from the Energy Research Center of the Netherlands (ECN, now part of the Netherlands Organization for Applied Scientific Research (TNO) [8,9]) for a 12-m long blade. Much later, the wind-energy department of the Danish Technical University (DTU) [10–12] investigated the transition on a 38.8 m blade. A much more in-depth investigation is part of the current IEAwind Task 29 Trans-European project [13].

A blade of 14 m in length was investigated with respect to the laminar–turbulent transition by using hot films in [14–16]. Table 2 summarizes all published measurements of the conducted tests, and reports the laminar–turbulent transition measurements in field experiments. To summarize to our investigations, proceeding investigations only showed isolated results with no indication of any quantitative accuracy. Nevertheless, an open question remains concerning the mechanism of transition (triggered by Tollmien–Schlichting waves or by the so-called bypass mechanism) and the accuracy of location detection. This paper focuses on results from the most recent experiment on a 45.3-m long blade and, by combining two different methods (thermographic imaging and microphones), we established the quantitative reliability of both methods.

The paper structure is as follows: First, we describe the site, the used WT, its blade, and the measurement equipment. Then, a summary of 2D and 3D CFD investigations is presented. Results are reported for pressure distribution and sound-pressure level (SPL) in combination with thermographic pictures. Finally, a summary and some conclusions are given. The paper is finalized with our conclusions and an outlook for possible further research.

Table 2. Summary of field experiments on wind turbine (WT) blades dedicated to investigations of the laminar–turbulent transition.

Blade Length (Meters)	Year	Reynolds Number/Million	Reference
te: 12.05	1983	3 (estimated)	[9]
38.5	2009	3–5	[11]
14.5	2011	1–2	[15]
2.2	2014	0.5–1	[17]
45.3	2018	1–5	This paper

2. Experiment Setup

2.1. Aerodynamic Glove

2.1.1. Turbine and Site

Measurements were performed on a Senvion (formerly: REpower) MM92 WT. This WT has a rated power of 2 MW, at rated wind speed of 12.5 m/s, and the hub height is 100 m. This type of a WT was first delivered in 2005 and, since then, more than 3000 units have been manufactured. The rotor blades are of the LM45.3p type. Due to a nondisclosure agreement with blade manufacturer LM, we obtained a Computer Aided Design (CAD) file of the blade's outer surface that allowed CFD simulations of the blade for comparison with the measurements.

The test site is located at Eggebek, a former military airport, approximately 100 km to the north of Hamburg, and approximately 50 km to both the North Sea (to the west) and the Baltic Sea (to the east). According to the European Wind Atlas [18], the roughness class is 1.5. If a logarithmic wind profile is fitted, then $z_0 = 0.055$ m has to be used as the roughness length. Assuming a wind speed of 6 m/s, the difference by wind shear from $z_1 = 65$ m (glove at bottom position) to $z_2 = 135$ m (glove at top position) is then only 0.38 m/s or 6.3%. Data acquisition took place on 13 July 2018, from 9:00 to approximately 13:00 local time.

2.1.2. Overview of Experiment Setup

The experiment setup consisted of different measuring techniques. First, an aerodynamic glove was used for measuring pressure distribution and the acoustic properties of the boundary layer together with environmental parameters like temperature, humidity, and the local acceleration of the glove. In addition, a five-hole probe was mounted onto the glove to determine local flow velocity. Second, thermographic flow visualization was applied by two teams (Deutsche WindGuard Engineering (DWGE) with the Bremer Institute for Metrology, Automation, and Quality Science (BIMAQ) and the German Aerospace Center (DLR)) to optically determine the laminar–turbulent transition of the boundary layer. The thermographic setups are described in detail in Section 2.2.1. In addition, a video camera was installed on the spinner and directed at the aerodynamic glove to measure the blade's vibrations.

Furthermore, the Supervisory Control and Data Acquisition (SCADA) data from the WT were given to us for a complete dataset during the measurement period. All clock times given in this article refer to local WT (SCADA) time.

2.1.3. Aerodynamic Glove

The principle of the aerodynamic glove is well-known in aviation experiments for measuring local flow conditions around the wings of an airplane [6]. For WT measurements, only a few experiments were conducted [10,11,15,16,19]. For this study, a local company that specializes in WT maintenance was commissioned to build the outer shell of the glove.

The surface consisted of carbon fiber fabrics, laminated onto 20-mm thick foam plates that were aligned to a blade that is identical to the one investigated to ensure the best possible fit. Foam plates allow the installation of tubes and cables in trenches below the glove's surface without damaging the blade, while maintaining the blade's profile.

In order to determine the local condition of the boundary layer, i.e., laminar or turbulent, 48 microphones were equally spaced along a straight line with an inclination of 20° with respect to the chord to minimize the influence of microphones upstream. Four microphones were positioned on the pressure side, one at the leading edge (LE) of the glove, and the remaining 43 on the suction side.

For determination of the pressure distribution along the suction side, 57 pressure holes were drilled into the glove. Of these, 48 holes were distributed exactly like the microphones, and the remaining nine holes were drilled at the center between two holes at the front of the glove, resulting in higher spatial resolution around the LE of the glove. For acquisition of the pressure data, a Digital Temperature Compensation (DTC) Initium from Esterline Pressure System was used. Figure 3 shows the distribution of the measurement points along the profile of the glove.

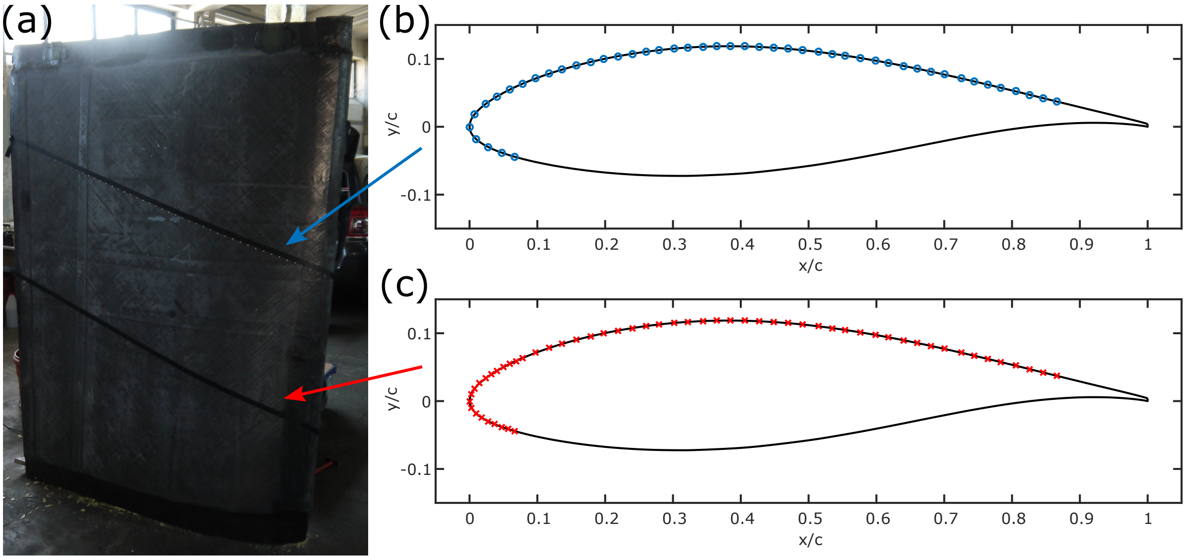

Figure 3. Position of sensors: (**a**) positions on the glove; (**b**) position of microphones; (**c**) positions of pressure holes.

Local flow velocity was measured by a five-hole probe. The data were also recorded by the Initium system. The five-hole probe was calibrated in the wind tunnel of the University of Oldenburg, Germany.

For data acquisition, a fanless computer was used. It was equipped with a WiFi access point to allow control of the system from the ground. The microphone data were recorded at 25 kHz and stored locally on four solid-state disks (SSDs). Acceleration, temperature, and humidity were also recorded at 25 kHz and stored in a separate SSD. The Initium data were recorded at 250 Hz and stored in the internal SSD of the computer via a LabVIEW program. This program was also used to synchronize all measurements. The power supply was realized by a battery with 24 V and 30 Ah. Figure 4 shows the data-acquisition system mounted on an aluminum plate ready to be mounted onto the pressure side of the glove. There is obviously an influence of the box on the pressure side on the flow of the suction that was investigated. Using 2D and 3D CFD (see Section 3), we were able to investigate the different pressure distributions on the suction side. The differences seen there were within the accuracy of the observed values.

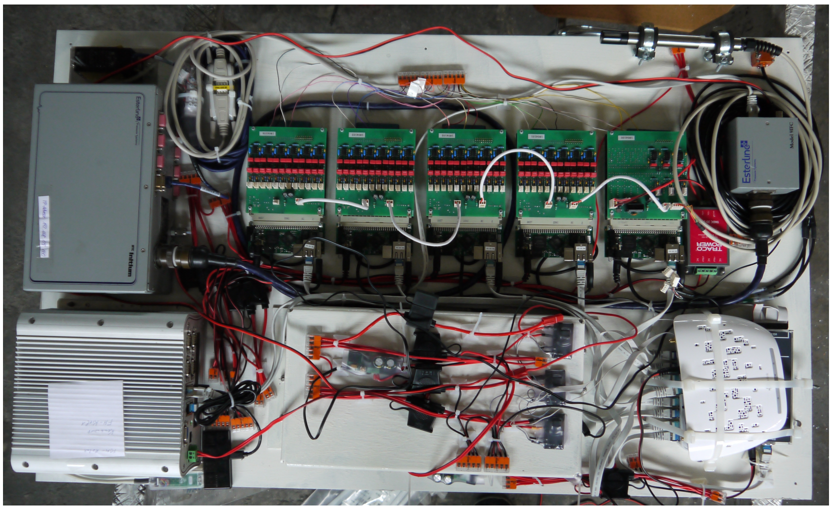

Figure 4. Data-acquisition system. Length, about 1 m.

2.2. Thermography

A thermographic measurement of the rotor-blade surface enables a noninvasive spatially resolved determination of the boundary-layer state. The method is called thermographic flow visualization. The measuring effect is based on an existing temperature difference between the flow and the rotor blade. The local surface temperature of the rotor blade depends on the local flow-related heat transfer coefficient. [20,21]. This results in a thermal fingerprint that correlates with the friction coefficient of the different flow areas of the boundary layer. Surface areas with laminar flow appear comparatively warmer in the thermographic image than surface areas with turbulent flow. This enables a distinction of the boundary layer flow areas and a localization of the laminar-turbulent transition, which can be realized by image processing algorithms [22,23]. Furthermore, advanced image processing methods enable the identification of flow separations [24].

Thermographic measurements for flow visualization have long been used in wind-tunnel tests. Whereas initially only experiments under ultra- and hypersonic conditions were thermographically accompanied, over time measurements in transonic and subsonic flows were also established [25]. Typical applications in wind-tunnel experiments are the localization of the laminar–turbulent transition and the identification of laminar or turbulent flow separations [26,27]. In addition, the measurement method was transferred to the free field to localize the laminar–turbulent transition on aircraft wings [28] and helicopter rotors [29] for flight tests under real conditions. The potential for localizing the transition on rotor blades of wind turbines has also already been proven [30]. However, a validation by means of simultaneous reference measurements has been missing so far.

In this study, different thermographic cameras were used in order to determine the laminar–turbulent transition on the aerodynamic glove and to assign the position to the three-dimensional geometry. This allowed a comparison with the other sensors by chord-based position information.

2.2.1. Thermographic Setup Provided by BIMAQ and DWGE

For the thermographic measurements performed by BIMAQ and DWGE, a cooled thermographic focal-plane-array detector from the manufacturer InfraTec (model ImageIR 8300) was used. The detector material is indium-antimonide. The 640 × 512 pixels detector is sensitive between 2 and 5 µm, the dynamic range of the camera is 14 bits, and the integration time can be set between 1 and 20,000 µs. InfraTec specifies the noise-equivalent temperature difference (NETD) as less than 25 mK @ 30 °C. The camera was calibrated by several measurements of a black-body radiator at different temperatures. The nonuniformity of the individual pixels was compensated by a one-point correction immediately before the presented measurements. A 200 mm telephoto lens with an instantaneous field of view (IFOV) of 0.08 mrad was used. This resulted in a spatial resolution of 11.2 mm for the given measurement distance of 140 m. The thermographic camera was triggered by an optical trigger mechanism. This allows a drastic reduction of the amount of data, since images are only taken when a rotor blade is in the camera's field of view. The subsequent evaluation of the thermographic data was done in Python. Figure 5 shows the experimental setup for the thermographic measurements at the Senvion WT.

The localization of the laminar–turbulent transition is performed by an approximation of the chordwise temperature profile on the rotor blade surface with a Gaussian cumulative distribution function. The approximation allows the determination of the transition position with subpixel accuracy [22]. By taking into account the position of the aerodynamic glove in relation to the thermographic camera, the visible surface area could be assigned to its geometry. With the known measurement distance, the pitch angle, and the local twist angle, several coordinate transformations are performed to enable the calculation of the angle of aperture resulting in the imaging of the surface of the aerodynamic glove. Based on the transition position in the image, the position on the surface of the aerodynamic glove can be determined in world coordinates and, finally, the position relative to the chord-length (x/c) can be found [30].

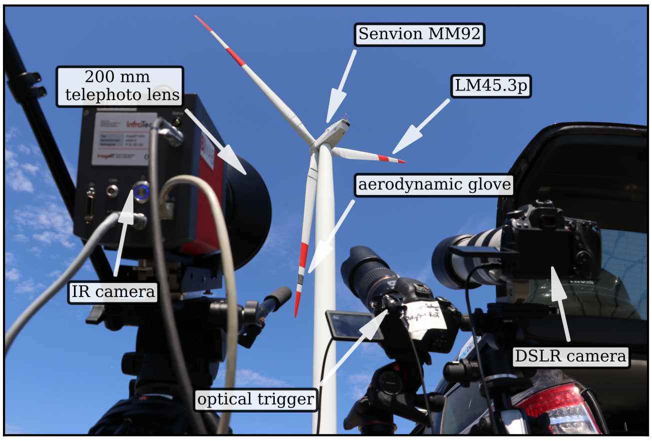

Figure 5. Experimental setup for thermographic flow visualization measurements. Foreground: thermographic camera with 200 mm telephoto lens, optical trigger, and DSLR camera for documentation purposes.

2.2.2. Thermographic Setup Provided by DLR

The second infrared camera setup was provided by the DLR and installed at a sufficient distance of approximately 80–85 m downstream of the WT mast to have an unobstructed view of the suction side of the aerodynamic glove at the minimum height above ground level (Figure 6). Thermal images taken shortly before the blade disappeared behind the mast offer the best possible spatial resolution at the given test conditions. Moreover, any distracting sunshine reflections can simply be avoided this way due to near vertical blade alignment.

For the thermographic measurements performed by DLR, a LWIR camera from the manufacturer IRCAM (model Equus 327k L) was utilized. The cadmium–mercury–telluride focal-plane-array detector with 640 × 512 pixels is sensitive in a spectral range between 8.0 and 9.4 μm and has a pixel pitch of 24 μm. A nominal exposure time of 100 μs at the highest frame rate of 105 Hz in free-running mode was applied without image triggering or averaging. To improve spatial resolution, the camera was equipped with an infrared STRIX 200 mm LWIR telephoto lens with a focal length of 200 mm and an aperture of F/1.4, enabling a maximum resolution of approximately 125 pixels per chord width (=83.3 px/m or 12 mm/px). This spatial resolution is marginally satisfactory for transition detection. A higher spatial resolution is simply invaluable at these long distances, because prices for IR lenses exponentially increase with focal length. The required difference in temperature between the glove's surface and the flow was facilitated by naturally preheating the blades by the sun.

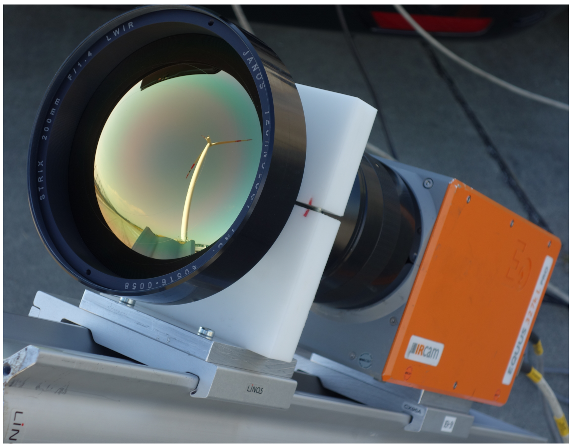

Figure 6. Thermographic setup provided by German Aerospace Center (DLR): thermographic camera Equus 327k L equipped with STRIX 200 mm LWIR telephoto lens.

2.3. Optical Camera

At the spinner of the WT, a video camera was mounted and directed toward the pressure side of the aerodynamic glove. Due to the curvature of the blade, it was not possible to observe the suction side of the glove. The camera was intended to visually detect vibrations of the blade, which, in turn, could be correlated to oscillations of local acceleration. Potential disturbance from precipitation, insects, or birds could be observed. Heating up of the blade and the aerodynamic glove from varying sun radiation could also be assessed in the blade positions that were out of sight for the stationary thermographic cameras. The optical camera is a JVC GZ-RX115BE camcorder. The camera was mounted onto the spinner with a rack that kept the camera firmly in place. Contained in this rack was an additional battery pack that allowed about 24 h of continuous operation. The camera was not remotely controlled. Instead, the recording was started before the WT was started, and the camera recorded during the whole test. The optical camera recorded with a rate of 50 frames per second. Picture resolution was 1920 × 1080 pixels.

Figure 7 shows that, in a WT standstill (pitch angle approximately 90°), the camera points toward the pressure side of the blade. In operation at low wind speeds (pitch angle approximately 0°), the camera points toward the trailing edge (TE) and the pressure side of the blade. At low pitch angles, the spoiler on the pressure side of the blade root becomes visible. Since the blade is flexible, the view varies with the out-of-plane bending of the blade (driven by thrust forces) and the in-plane bending of the blade (mainly driven by gravitational force, i.e., determined by rotor position). The optical camera has a focal length range from 2.9 to 116 mm. Therefore, the aerodynamic glove could have been observed from much closer. However, the intention was to also observe the blade around the aerodynamic glove. The high resolution of the pictures allows zooming into the videos if necessary for assessing certain scenarios, for example, during the start-up (SU) phase.

Figure 7. View from optical camera on the spinner of the pressure side of the blade at R = 35 m. Black box contains the entire data-recording system, including power supply. Chord there is 1.5 m. In addition, orientation of the five-hole probe relative to vertical axis (approximate rotor plane) indicates the instantaneous pitch to be compared with values from the Supervisory Control and Data Acquisition (SCADA) system. (**Left**) WT in standstill; (**Right**) WT in operation.

3. Computational Fluid Dynamics

3.1. Set-Up

For 2D investigations, we used Xfoil [31], a simple panel-code enhanced by methods from interactive integral boundary layer theory and a data-based e^N-method to predict laminar to turbulent transition. Default settings (200 panels for example) were not changed, aside from the N-factor, which was set to N = 3 to account for higher inflow turbulence when compared to wind-tunnel measurements.

DLR-FLOWer [32] was used in 2D-mode to compute a c_f (friction coefficient)-distribution (see Figure 8).

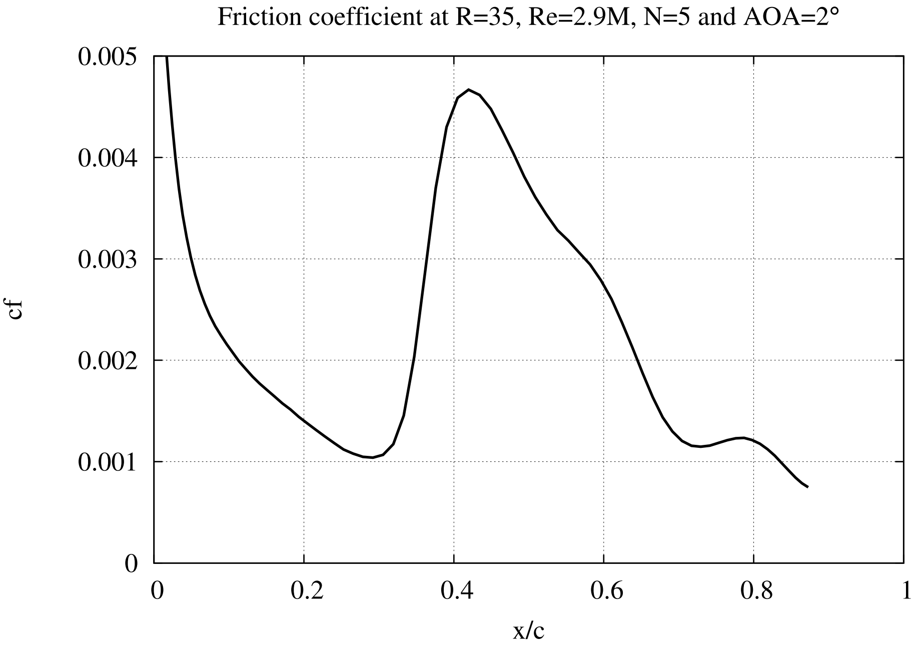

Figure 8. Location of transition from wall shear stress (c_f) by CFD code FLOWer. $N = 5$ corresponds to a TI (TI) of 0.3%. Onset of transition may be located at $x/c = 0.29$, and flow is fully turbulent at $x/c = 0.42$. Slope is at maximum at $x/c = 0.36$.

A structured quad-mesh of 336 × 72 cells was used with y^+ less than 1 and the extension of the computational domain was approximately 100 chord lengths. Wilcox turbulence (number 13 in FLOWer's list) was used.

All 3D simulations wer performed using DLR's TAU-code [5].

Three sets of meshes were generated:

1. low: 996 k tests + 149 k prisms
2. medium: 853 k tets + 149 k prisms
3. high: 4158 k test + 1744 k prisms

DLR-TAU's built-in mesh quality tool (setup-taugrid) was used to investigate the quality of the mesh. It locally and globally calculates in index $0 < index < 1$. The first two sets had indices less than 0.8 for the worst cells, but with the final mesh, the worst cells improved to an index of 0.24.

A final unstructured mesh consisting of 1.7 million points was prepared with ICEM/CFD, a meshing tool. To resolve the boundary layer down to $y^+ < 1$ 20, additional layers of prisms were added so that the final mesh consists of four million tetrahedron and 1.7 prisms. Spalart–Allmeras SAO turbulence model was used. The extension of the computational domain was -50 m < x < 50 m in main flow direction and -30 m < $y(z)$ < 30 m in the others.

No further mesh refinement or coarsening was performed.

3.2. Results from CFD

Parallel to the preparation of the experiments, 2D (Xfoil) and 3D (DLR-TAU) CFD simulations were performed as described before. First, a 2D simulation was performed using Xfoil [31]. In Figure 9, the resulting Lilienthal polar of that section is shown. A so-called laminar nose, a region of small drag, $c_D < 0.008$, is clearly visible. Using a tangent, an operating point of the airfoil $(\alpha_{des}, c_{L,des})$ can be determined at the largest lift-to-drag ratio $c_{L,des}/c_{D,des}$. However, this does not necessarily means, that the blade designer used this procedure as many other constraints have to be includes. Our experimental findings (see Section 4.2) indicate a somewhat higher angle of attack (AOA) at 9 rpm. Figures 2 and 10 (right side) show the (2D) pressure distribution on the surface of the profile for an AOA of $\alpha_{des} = 3.5°$ at operating conditions. It is clearly seen that no flow separation was present there. It has to be noted that, for every CFD calculation, including laminar to turbulent transition, an additional quantity, the N-factor, has to be provided. From wind-tunnel measurements, it is common practice to relate N to inflow turbulence intensity (TI) by Mack's relation:

$$N = 2.13 - 6.18 \cdot \log_{10}(TI) \ . \tag{1}$$

Mack [33,34] recommended to use it in region $0.1\% < TI < 1\%$. Here, TI comes from $TI = \sigma/\overline{v}/ = (\int v^2 P(v)dv)^{1/2}/\int vP(v)dv$, i.e., standard deviation divided by average wind speed for some ensemble. Note that Equation (1) cannot be used in atmospheric flow without further assumptions. A procedure on how to extend Mack's correlation was proposed in [15].

Furthermore, full 3D simulations were used to estimate the position of transition from laminar to turbulent flow in the boundary layer on the suction side of the glove. Figure 10 (left) shows the expected flow state regions obtained via DLR-TAU code [5], a CFD code by the DLR. Blue corresponds to laminar flow, while red indicates fully turbulent flow. A transition line is seen around $x/c = 0.3$ (c = total chord = 1.5 m) in the central region of the glove. Due to boundary effects, the transition is forced more to the LE at the border of the glove.

In addition, perturbation of the flow due to the box on the lower side of the glove was investigated and has been seen a posteriori to be within the variation due to surface imperfections. Figure 10 (right) shows the 3D pressure distribution. Again, as for the transition, smooth variations as expected from 2D were visible in the central part where the pressure sensors and the microphones had been placed. From these investigations, we can conclude that, even under ideal conditions, a laminar extension of the suction side not longer that 40% can occur.

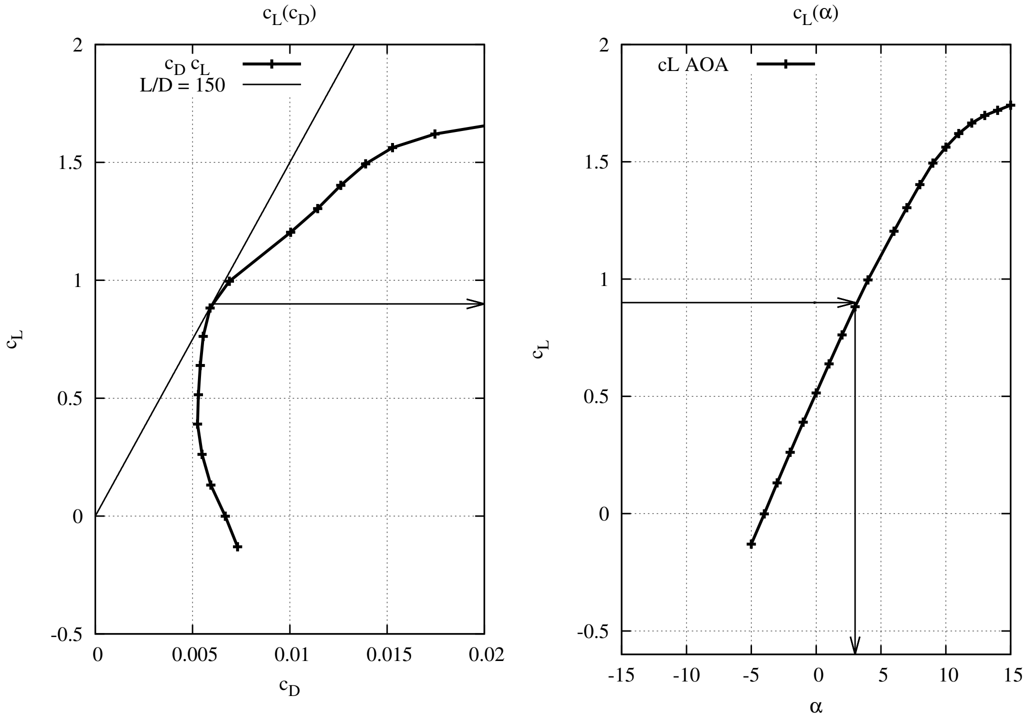

Figure 9. Lilienthal polar of the profile at the location of the glove (Reynolds number, four million). Left side: Lift versus drag. Right side: Lift vs angle-of-attack A so-called laminar nose, a region of small drag $c_d < 0.008$, is clearly visible. Arrows indicate the determination of the operation point using a tangent. N-factor was set to 3. By Mack's correlation, this corresponds to an inflow turbulence of 0.7%. We assume this to be the aerodynamic relevant part of the whole tubulence spectrum.

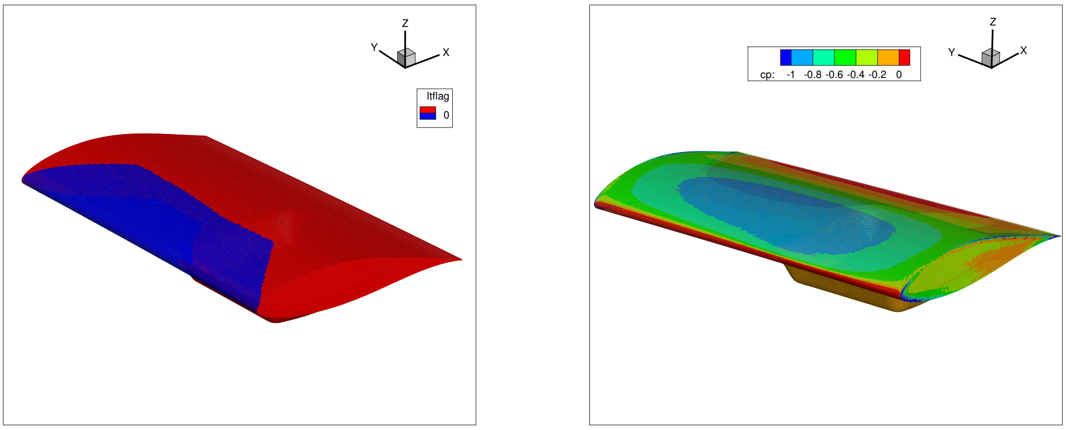

Figure 10. (**Left**): Estimated flow state regions from 3D transitional computational fluid dynamics (CFD), DLR -TAU code). (**Blue**) Laminar flow; (**Red**) fully turbulent flow. (**Right**): Static pressure coefficient.

4. Measurement Results

4.1. Measurements

Now, results are discussed in more detail in order to present a complete picture of the aerodynamic properties of the boundary-layer flow around the glove.

Two different datasets are compared, the SU of the WT (dataset 11:01) and the steady-state (SS) of the WT (dataset 11:18). These two datasets were exemplarily chosen to illustrate the different operation states. All measurements were performed on a single sunny day over a time period of about 4 h. First, six sequences, each 60 s long, were recorded in a stand-still configuration with the brakes of the turbine tightened. After that, the brakes were loosened, and the turbine was started. Thirty-one sequences, 60 s in length and a delay of 30 s in between, were recorded. During measurements, the turbine was stopped and started again in order to measure the SU of the turbine, as well as the SS. The goal was to find differences between the different operation states to study the temporal evolution of the boundary-flow conditions.

While the measurement system in the glove recorded data continuously, the thermography cameras recorded stationary images of the glove at a fixed position of the blade's revolution.

4.2. *Inflow*

First, the inflow obtained by the five-hole probe is discussed. Due to the calibration of the probe in the wind tunnel of the University of Oldenburg, Germany, it was possible to obtain the inflow velocity together with the AOA. Figure 11 shows both quantities of the flow for the different operation states, respectively.

It can be seen that, for SU, the AOA increased from negative to positive values, as expected. In addition, an offset between the inflow velocity obtained by the probe (blue) and by the SCADA data (red) can be seen, which is explained by the different locations where the wind speed was measured.

For SS, the variation of the AOA was much smaller, and no drift was observed. The offset between inflow velocities was no longer observed. Furthermore, inflow velocity varied along the revolution of the blade, which is a direct confirmation of the atmospheric layering.

Obviously, the measured AOA (5°) does not match with with values from Table 1. The reason is not clear and has to be discussed with the designer of the blade.

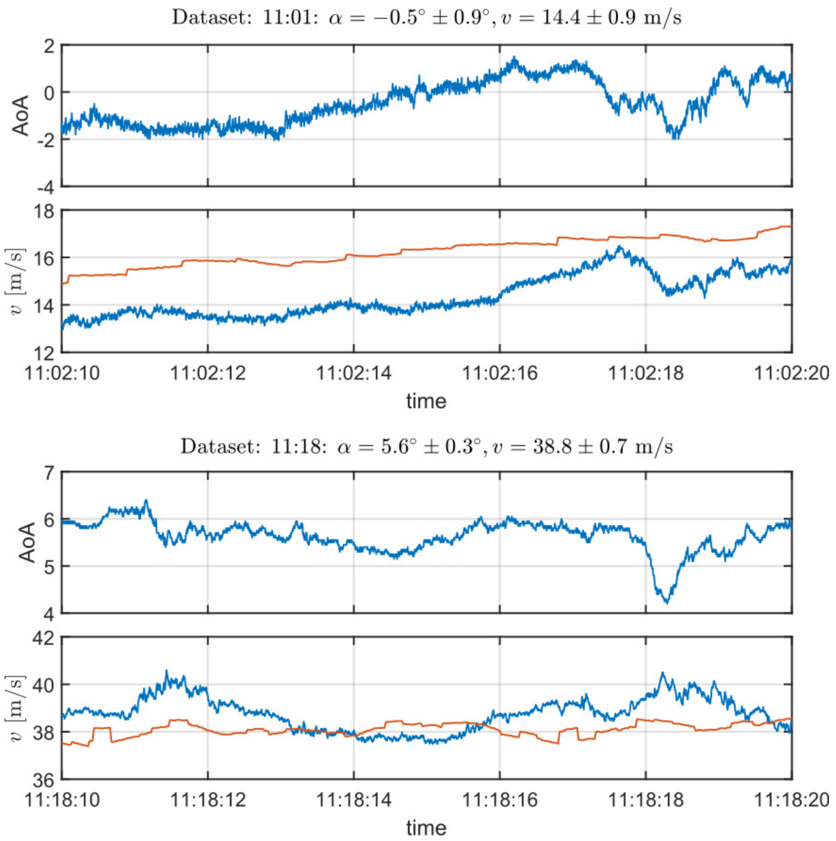
Dataset: 11:01: $\alpha = -0.5° \pm 0.9°, v = 14.4 \pm 0.9$ m/s

Dataset: 11:18: $\alpha = 5.6° \pm 0.3°, v = 38.8 \pm 0.7$ m/s

Figure 11. Inflow properties of different operation states. (**Top**) Start-up (SU); (**Bottom**) steady state (SS). Shown are AOA (**Upper row**) and inflow velocity (**Lower row**). (**Blue**) Velocity obtained by five-hole probe; (**Red**) velocity obtained by SCADA data.

4.3. Pressure Distribution

Furthermore, pressure distribution on the glove was measured. For a better comparison, the same 10 s sequence as in Figure 11 was used. The recorded pressure was averaged and, using:

$$c_p = \frac{2(p - p_0)}{\rho v^2}, \tag{2}$$

lift coefficient c_p was calculated. Figure 12 shows the resulting distribution of c_p for both operating states. For comparison, the CFD results of Xfoil calculations with a different AOA are also shown.

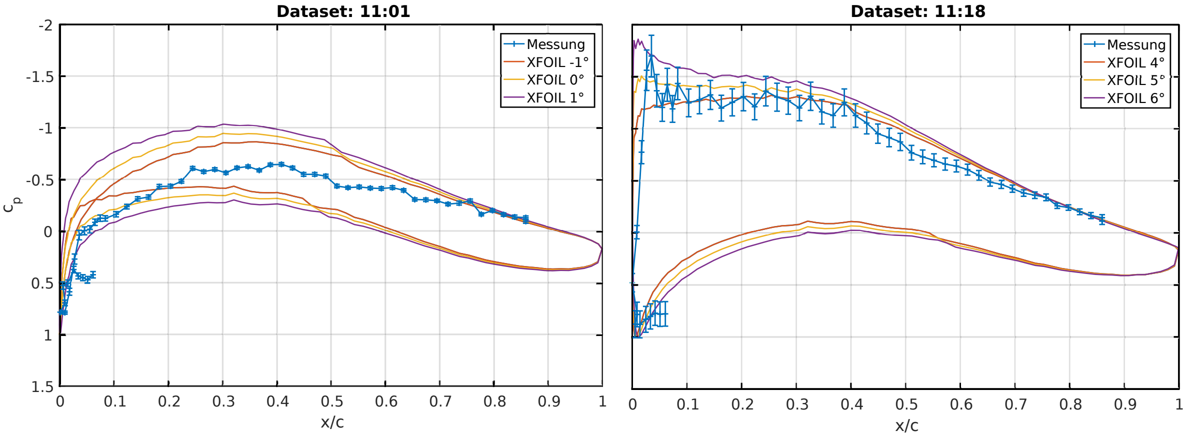

Figure 12. Pressure (c_p) distribution on the glove. (**Left**) SU; (**Right**) SS.

For SU, poor agreement was found, which might have resulted from the transient character of the sequence. The AOA increased from $-1°$ to $+2°$, which made a comparison with a stationary AOA somewhat difficult.

For SS, better agreement between measurement and CFD was observed. The measured AOA of the five-hole probe of 5.6° (cf. Figure 11) was in good agreement with the observed c_p distribution.

It is worth noting that, for both states, pressure distribution on the pressure side of the glove differed from the CFD calculations. Since pressure distribution is strongly dependent on the local curvature at the LE, small deviations of the glove's shape result in large changes to the lift coefficient.

Too-high production costs for a glove with wind-tunnel (or even commercial-blade) quality prevented a smoother surface. Hence, part of the observed deviations might be explained by insufficient surface quality.

4.4. Detection of Transition Position

In addition to pressure distribution, determining the flow character of the boundary layer was a main goal of this project. Therefore, the noise emission on the suction side was recorded by the 48 microphones.

The determination of the transition position was performed as described in [10]. First, the power spectral density of the pressure signal from the microphones $\widetilde{p(\omega)}$ was calculated from time series $p(t)$ by applying:

$$\widetilde{p(\omega)} := \frac{1}{2\pi}\int_{-\infty}^{+\infty} r_{pp}(t)\cdot e^{-i\omega t}\,dt\,, \tag{3}$$

$$r_{pp}(t) = \lim_{T\to\infty}\frac{1}{2T}\int_{-T}^{+T} p(\tau)p(\tau+t)\cdot d\tau\,, \tag{4}$$

assuming a real time signal. Furthermore, [10] used only a finite part of the spectrum:

$$p^2_{cut} = 2\int_{\omega_1}^{\omega_2} \widetilde{p(\omega)}\, d\omega, \tag{5}$$

with $[f_1; f_2]$=[2 kHz; 6 kHz], $\omega = 2\pi f$ and $p_{ref} = 20$ µPa. Relevant SPL L_p^{cut}, then, was determined by:

$$L_p^{cut} = 20\log_{10}\left(\frac{P_{cut}}{p_{ref}}\right)(dB)\ . \tag{6}$$

By definition, SPL is given in pseudo-dB units of Decibel. In order to study the temporal evolution of the SPL, sequences of 2048 data points were averaged and the SPL for this sequence was calculated, resulting in a time resolution of 12 Hz. Figure 13 shows the temporal evolution of the SPL for both operating states, together with local radially outward-directed acceleration.

The color map changes from blue via green and yellow to red with increasing values of SPL. The overall value of the SPL was lower in the SU than in the SS. Furthermore, areas with higher SPL could be found at the back part of the suction side that traveled in the direction of the LE.

In the SS, the overall value of SPL was higher. In addition, a distinct region at the LE could be recognized with much lower SPL values. This is a characteristic of a laminar-boundary layer, while most of the suction side has a turbulent boundary layer, resulting in high SPL values.

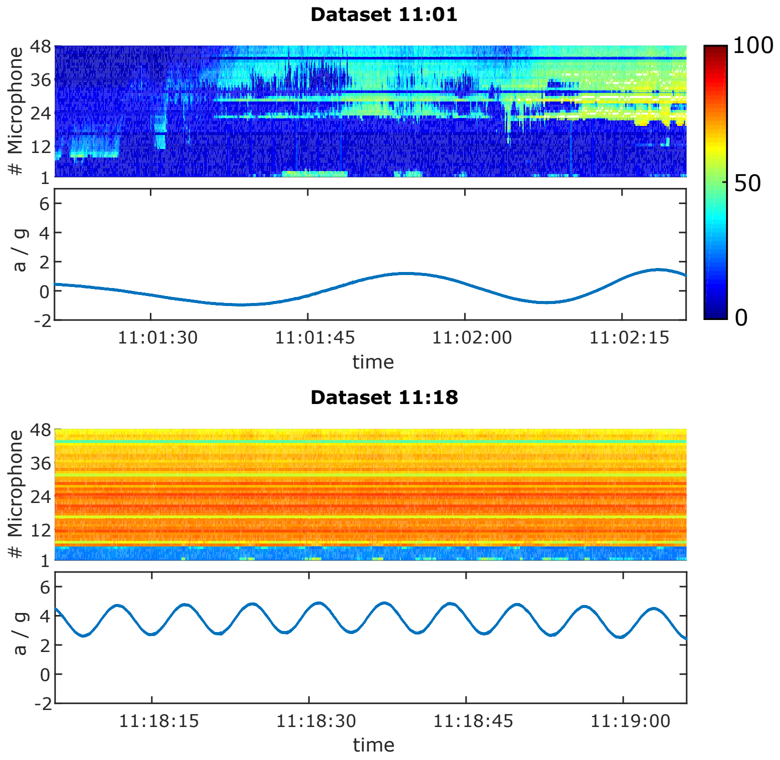

Figure 13. Detection of the transition position. (**Top**) SU; (**Bottom**) SS. (**Upper row**) Sound-pressure level (SPL) in Decibels (dB). (**Color map**) Dark blue corresponds to 0 dB and red to 80 dB. (**Lower row**) Local acceleration.

Furthermore, a small periodic variation of the transition position could be observed. Due to the periodic variation of the local acceleration, the blade position relative to the ground could be determined. At the lowest point of the revolution, gravity and centrifugal force were pointing in the same direction, resulting in a maximum acceleration. At this position, the transition position was moving slightly in the direction of the LE. Since the blade passes through the wind shadow of the tower, higher inflow turbulence is expected, thus resulting in a more turbulent boundary layer.

4.5. Thermography Team BIMAQ and DWGE

As an example, the results from 11:15:32 and 10:16:45 (SCADA time) are shown. Figure 14 shows the transition position (Team BIMAQ and DWGE uses location of maximum temperature gradient to locate a transition point) derived by the image-processing algorithm from Dollinger et al. [22] for the SU phase of the WT. On the left side, the thermographic image with the visible LE and TE, as well as derived relative transition position p_{tr}, are shown. On the right side, surface temperature T of the glove at the location of the microphones is shown as a function of the position on chord x/c, determined by a previously performed geometric assignment [30]. The span-wise average transition position along the glove is $\bar{x}_{\mathrm{tr,\,IR}}/c = 0.337$, with large local fluctuations due to turbulence wedges as a result of the high surface roughness of the aerodynamic glove. Locally at the location of the microphones, the transition position determined by the thermographic flow visualization was $x_{\mathrm{tr,\,IR}}/c = 0.255 \pm 0.003$. Uncertainty of the measurement was estimated according to [30]. This result is consistent to the transition location deduced by the microphone data, $x_{\mathrm{tr,\,M}} = 0.26 \pm 0.01$ (cf. Figure 15).

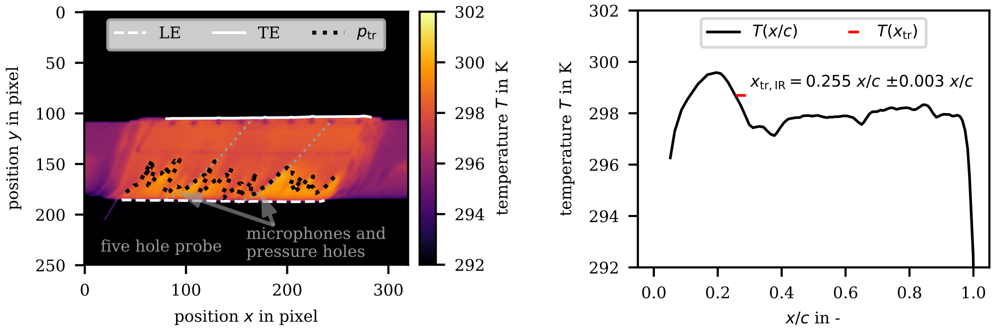

Figure 14. Thermographic flow visualization measurement at 11:15:32 (SCADA time). **Left**: Thermographic image. **Right**: x-y-plot of temperature.

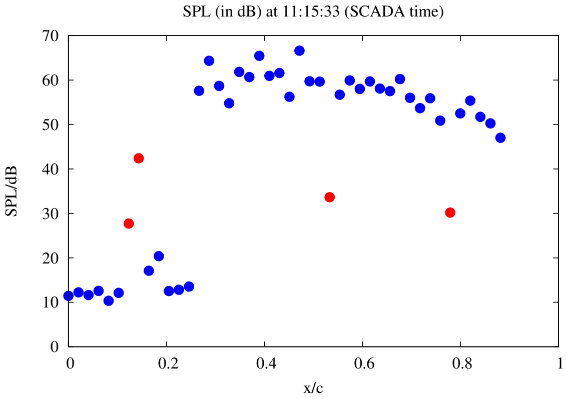

Figure 15. Development of SPL (in dB) vs. chord at 11:15:32 (SCADA time). If one discards outliners (in red) $x_{\mathrm{tr,\,M}}/c$, may be deduced to $x_{\mathrm{tr,\,M}}/c = 0.26 \pm 0.01$.

In Figure 16, the results for the turbine in regular operation mode are shown. Again, on the left, the thermographic image of the glove is shown, and on the right, surface temperature T is depicted as a function of chord-wise position x/c. Besides the relative position of the transition in image p_{tr}, the visible LE and TE are shown. Due to a reflection of sunlight on the surface of the glove, the area toward the TE appears very warm. This area was not included in the image processing for the evaluation of the transition position. The span-wise average transition position for this measurement was $\bar{x}_{\mathrm{tr,\,IR}}/c = 0.048$, and the transition position at the location of the microphones was $x_{\mathrm{tr,\,IR}}/c = 0.039 \pm 0.004$. From the microphone data, here, we obtained a slightly larger value of $x_{\mathrm{tr,\,M}}/c = 0.05 \pm 0.01$. Note that the spacing of the microphones was 0.02 (in x/c units).

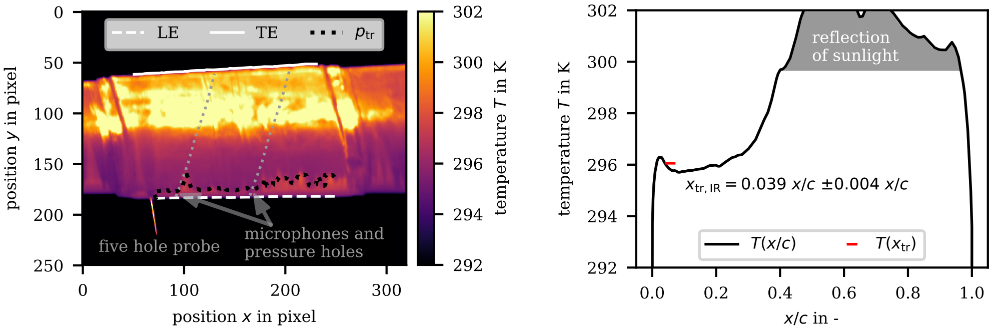

Figure 16. Thermographic flow visualization measurement at 10:16:45 (SCADA time). **Left**: Thermographic image. **Right**: x-y-plot of temperature.

Obviously, a rough surface leads to a premature laminar–turbulent transition near the LE during these operational conditions.

4.6. Results Team DLR

As described above, the detection of boundary-layer transition on rotating blades relies on the increase in the heat-transfer rate between flow and blade surface that occurs when the boundary-layer state changes from laminar to turbulent. The change in heat-transfer rate causes differences in blade-surface temperature that were measured by an infrared camera.

Thus, transition detection was based on analysis of single instantaneous thermal images of the rotating blade in the SU phase, indicating different stages of surface-temperature evolution from the initially quasi-uniform to a final local-equilibrium distribution. Image preprocessing here includes bad-pixel elimination, sky–background separation, and contrast enhancement. Figure 17 shows two typical thermal images obtained correspondingly at 11:22:27 and 11:23:13 (SCADA time) during a single WT run, accordingly preprocessed. The rotation direction here was from left to right, and the cold-sky background was colored maroon to enhance the visibility of the WT parts presented in graduations of gray. The vertical gray-scaled area on the right side of the picture represents the mast of the facility. The areas with laminar (warm/bright) and turbulent (cold/dark) boundary layers on the glove surface could clearly be distinguished in these pictures. Variations of the rotation rate (from 4.0 to 8.5 rpm) and of the blade pitch angle (from 2° down to 1°) taking place between both these time instances during the SU phase caused the shifting of the transition region in the thereby documented time.

In the next step, DLR software *HeatFIT* was used for the final conditioning and automatic marker-based 3D reconstruction of the thermal images with subsequently mapping of the data values onto the 3D grid of the aerodynamic glove (Figure 18). The geometric information necessary for the markers was provided by the CFD model. Full computerized analysis of temperature distribution on the test surface in accordance with the method introduced by Schülein [35] allowed the distinction between the starting points and the end points of the transitional region. Additionally, in a simplified approach, the transition zone between laminar and turbulent flows was detected as a border line that corresponds to the locations with the highest wall-temperature gradients (highest gradients of thermal-image intensity) measured in the streamline direction (areas with detected laminar flow are highlighted in yellow in Figure 19). Figure 20 shows typical surface–temperature distribution (here, thermal-image intensity) over normalized coordinate x/c, extracted from the left thermal image in Figure 19, along the mid-line of the glove. This example demonstrates the mutual positions of points characterizing the transition zone: onset transition, end of transition, and highest temperature gradient. As described in [29] and seen in the presented example, the detected transition line in accordance with the highest-gradient criterion approximately corresponds to the midpoint of the transition zone. A comprehensive characterization of the transition zone facilitates comparison with the independently obtained results by different experiment methods and numerical simulations. The actual midpoints of the transition zone, detected in both thermal images along the microphone-array line, were found to be at $x_{tr,IR}/c = 0.370 \pm 0.005$, and 0.080 ± 0.005, very close to the transition locations detected by microphone-array method ($x_{tr,m}/c = 0.34 \pm 0.01$, see Figure 21, and 0.07 ± 0.01).

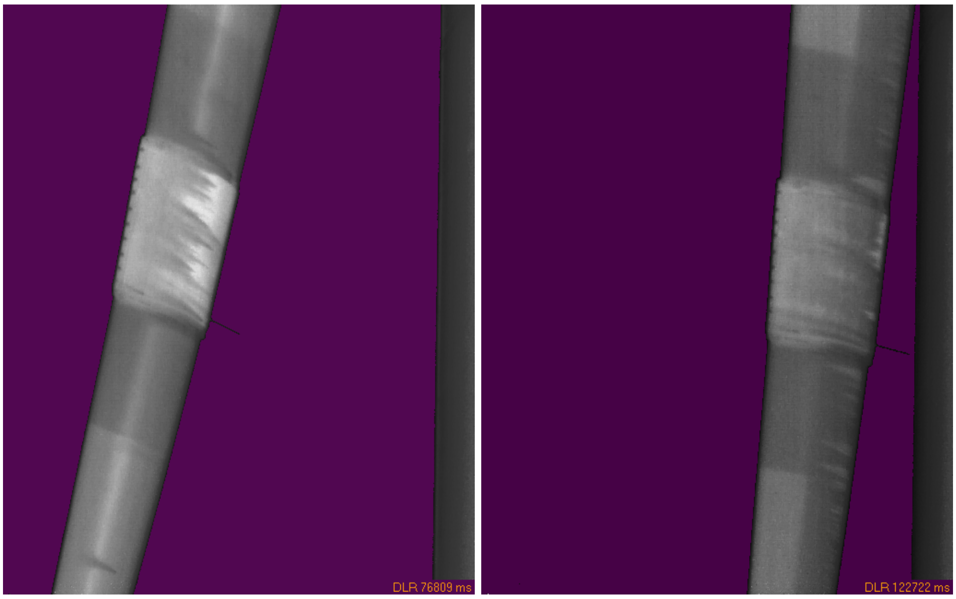

Figure 17. Two typical thermal images obtained by DLR setup after image processing including bad-pixel elimination, sky–background replacement, and contrast enhancement. Images are from 11:22:27 (**Left**) and 11:23:13 (**Right**), both SCADA time). Left shows more laminar parts during startup, and right only very small extended regions during constant rpm (approximately 9) operation mode.

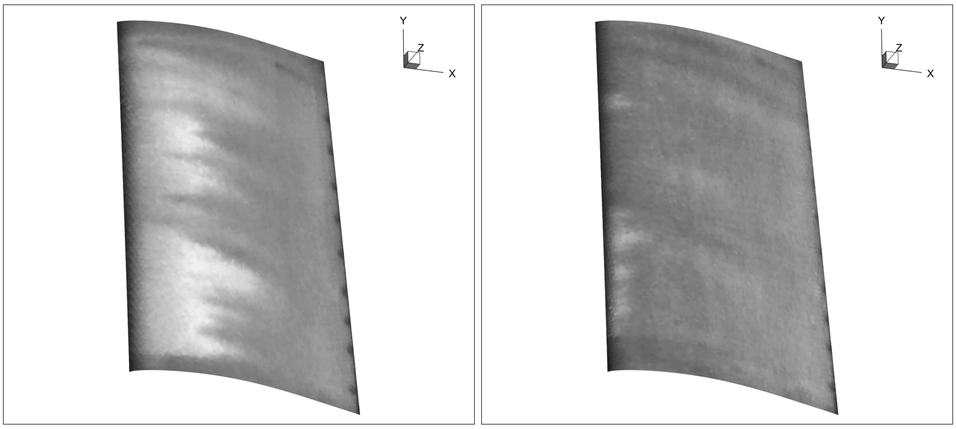

Figure 18. Thermal images from Figure 17 after reconstruction and mapping onto the 3D grid of the aerodynamic glove. Images are from 11:22:27 (**Left**) and 11:23:13 (**Right**), both SCADA time. Here, only the glove is shown.

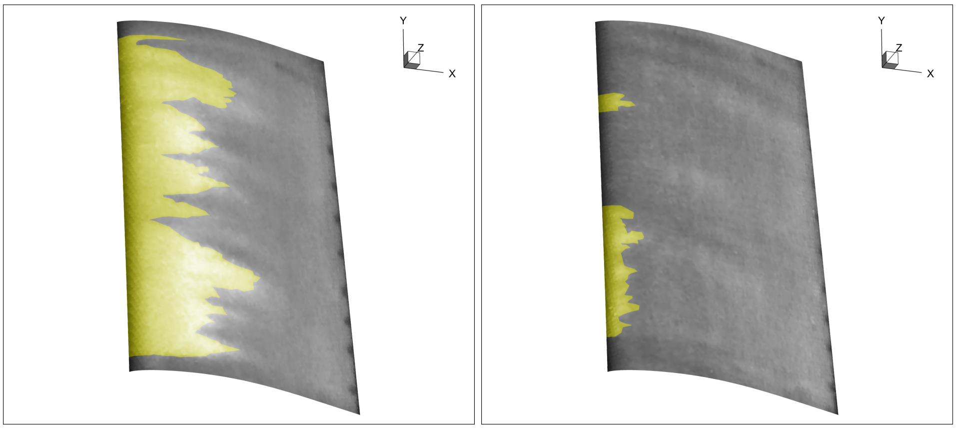

Figure 19. Thermal images from Figure 17 after transition-detection procedure. **Left**: Thermographic image. **Right**: x-y-plot of temperature.

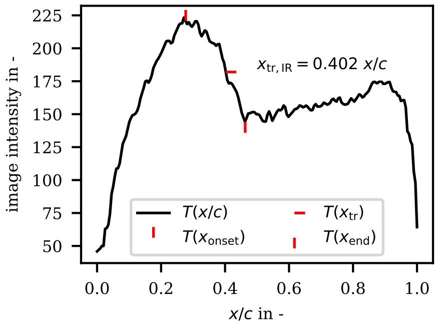

Figure 20. Thermal image intensity extracted along microphone-array line for time instance 11:22:27.

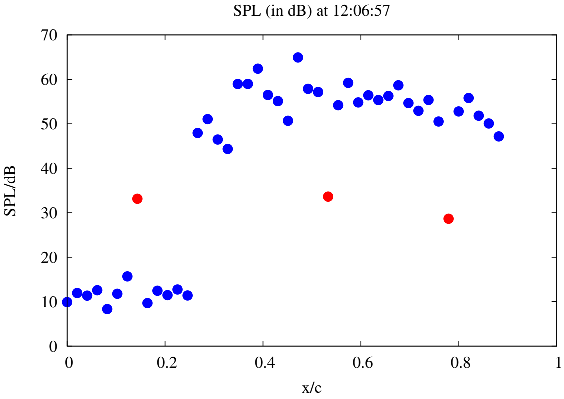

Figure 21. Development of SPL vs. chord at 12:06:57. If one discards outliers (in red), $x_{\mathrm{tr,\,M}}/c$ may be deduced to $x_{\mathrm{tr,\,M}}/c = 0.34 \pm 0.01$.

4.7. Discussion

The main objective was a quantitative comparison of the detection of laminar–turbulent transition positions with two different methods: thermographic pictures and microphones. It is interesting to note that both methods agree in their results, within their limitations: Thermography takes the maximum temperature gradient as the location of transition, as Figures 14 and 16 indicate. In contrast (see Figure 15), transition from SPL seems to be very sharp within one unit of distance (= $1/40 = 0.025$ in terms of x/c).

If one uses CFD (see Figure 8) to determine laminar–turbulent transition, then results compare more to a region with the end of the laminar part ($(x/c)_{lam-end}$= 0.29) given by the minimum of c_f, and the beginning of the fully turbulent region by the following maximum ($(x/c)_{fully-turb-start}$= 0.42).

Therefore, it can be stated that thermographic imaging provides a nonintrusive method that can be used from a distance to detect laminar–turbulent transition; its accuracy proved to be in accordance with the data both from microphones and transitional CFD.

5. Summary, Conclusions, and Future Research

An aerodynamic glove, known from free-flight experiments with an airplane, was designed, manufactured, and used on a 2 MW state-of-the-art WT to investigate the laminar–turbulent transition. Local inflow conditions were recorded by a five-hole-probe, and surface-pressure measurements were performed by an array of 64 pressure sensors from PSI-Initium. In addition, an array containing 48 microphones was used for capturing flow sound near the wall. Two different types of thermographic cameras were used to report the rotor-surface temperature and, thereby, distinguish the laminar (warmer) and turbulent (colder) regions. AOAs could be determined from the five-hole probe and pressure distribution within one degree of accuracy.

We now come to our main conclusion: Although the geometric surface did not meet the standards from the wind-tunnel models and, during the measurement, blade and glove seemed to be fouled by insects and/or dust, the irregularly shaped regions of the laminar boundary layer were consistently identified by thermographic imaging and the microphones, even during WT SU, and agreed within their respective accuracies of 1% or less.

In the future, the following investigations are planned:

- A new glove with a surface treatment in accordance at least with ordinary WT blades will be manufactured,
- microphones will be placed close to the tail to investigate noise emission,
- a small LIDAR device will be included into the glove,
- passive and active flow control devices will be investigated, and
- an LES (large Eddy Simulation) model will be developed with an inflow generator to simulated highly turbulent inflow to improve transition detection on WT blades by simulation.

Author Contributions: conceptualization, A.P.S. and T.R.; methodology, T.R and A.P.S; software, T.R. and A.P.S.; CFD, T.R., and A.P.S.; validation, T.R; formal analysis, T.R.; investigation, all; resources, C.D., N.B., E.S., and C.J.; data curation, T.R.; writing—original-draft preparation, T.R., C.D., and A.P.S.; writing—review and editing, T.R., A.P.S., and A.F.; visualization, T.R., C.D., and E.S.; supervision, A.P.S.; project administration, T.R.; and funding acquisition, A.P.S.

Funding: This research was funded by the Gesellschaft für Energie und Klimaschutz Schleswig-Holstein GmbH, Kiel, Germany, grant number 8/12-26.

Acknowledgments: We acknowledge the help from Senvion, Denker & Wulf, Wingtec, and others. We thank the University of Oldenburg and Jaroslaw Puczylowski, PhD for use of their wind tunnel for the calibration of the five-hole probe. Computations were performed with resources provided by the North German Superconducting Alliance (HLRN).

Conflicts of Interest: The authors declare no conflict of interest.

Abbreviations

The following abbreviations are used in this manuscript:

AOA	Angle of attack
BIMAQ	Bremer Institute for Metrology, Automation, and Quality Science
CFD	Computational Fluid Dynamics
DLR	German Aerospace Center
DTC	Digital Temperature Compensation

DWGE	Deutsche WindGuard Engineering GmbH
L2D	Lift-to-drag c_L/c_D
SCADA	Supervisory Control and Data Acquisition
SPL	Sound-pressure level
SS	Steady-state phase
SSD	Solid-state disk
SU	Start-up phase
TI	Turbulence intensity
TSR	Tip-speed ratio
WT	Wind turbine

References

1. Schaffarczyk, A. (Ed.) *Understanding Wind Power Technology*; Wiley: Chichester, UK, 2014. [CrossRef]
2. Schaffarczyk, A.P. *Introduction to Wind Turbine Aerodynamics*; Springer: Berlin, Germany, 2014.
3. Abbot, I.H.; von Doenhoff, A. *Theory of Wind Sections*; Dover Publications Inc.: New York, NY, USA, 1959.
4. Ceyhan, O.; Pires, O.; Munduate, X.; Sorensen, N.N.; Schaffarczyk, A.P.; Reichstein, T.; Diakakis, K.; Papadakis, G.; Daniele, E.; Schwarz, M.; et al. Summary of the Blind Test Campaign to predict the High Reynolds number performance of DU00-W-210 airfoil. In Proceedings of the AiAA SciTech Forum, Grapevine, TX, USA, 9–13 January 2017.
5. *TAU-Code User Guide, Release 2018.1.0*; Technical Report; Deutsches Zentrum für Luft- und Raumfahrt e.V., Institute of Aerodynamics and Flow Technology: Göttingen, Germany, 2018.
6. Seitz, A.; Horstmann, K.H. In-flight investigation of Tollmien-Schlichting waves. In *IUTAM Symposium on One Hundret Years of Boundary Layer Research*; Meier, G., Sreenivasan, K., Eds.; Springer: Dordrecht, The Netherlands, 2006; pp. 115–124.
7. Reeh, A.; Tropea, C. Behaviour of a natural laminar flow airfoil in flight through atmospheric turbulence. *J. Fluid Mech.* **2015**, *767*, 394–429. [CrossRef]
8. Van Groenewoud, G.J.H.; Boermans, L.M.M.; van Ingen, J.L. *Onderzoek naar de Omslag Laminar-Turbulent van de Grensllag op de Rotorblades van de 25 m HAT Windturbine*; Rapport LR-390; Technische Hogeschool Delft: Delft, The Netherlands, 1983.
9. Van Ingen, J.L.; Schepers, J.G. Prediction of boundary layer transition on the wind turbine blades using th e^N method and a comparison with experiment. Unpublished paper by private communication.
10. Troldborg, N.; Bak, C.; Aagaard Madsen, H.; Skrzypinski, W. *DANAERO MW: Final Report*; DTU Wind Energy: Lyngby, Denmark, 2013.
11. Madsen, H.; Fuglsang, P.; Romblad, J.; Enevoldsen, P.; Laursen, J.; Jensen, L.; Bak, C.; Paulsen, U.; Gaunaa, M.; Soerensen, N.N.; et al. The DAN-AERO MW Experiments. In Proceedings of the 48th AIAA Aerospace Science Meeting Including the New Horizons Forum and Aerospace Exposition, Aerospace Science Meetings, Orlando, FL, USA, 4–7 January 2010.
12. Madsen, H.A.; Özçakman, Ö.S.; Bak, C.; Troldborg, N.; Sørensen, N.N.; Sørensen, J.N. Transition characteristics measuremd on a 2 MW 80 m diameter wind turbine rotor in comparison with transition data from wind tunnel measurements. In Proceedings of the AIAA Scitech Forum, San Diego, CA, USA, 7–11 January 2019.
13. IEA Wind Task 29. Available online: https://community.ieawind.org/task29/home (accessed on 21 January 2019).
14. Schwab, D.; Ingwersen, S.; Schaffarczyk, A.; Breuer, M. Aerodynamic Boundary Layer Investigation on a Wind Turbine Blade under Real Conditions. In *Wind Energy—Impact of Turbulence*; Hölling, M., Peinke, J., Ivanell, S., Eds.; Springer: Berlin/Heidelberg, Germany, 2014; pp. 203–208.
15. Schaffarczyk, A.P.; Schwab, D.; Breuer, M. Experimental detection of laminar-turbulent transition on a rotating wind turbine blade in the free atmosphere. *Wind Energy* **2017**, *20*, 211–220. [CrossRef]
16. Schwab, D. Aerodynamische Grenzschichtuntersuchungen an einem Windturbinenblatt im Feldversuch. Ph.D. Thesis, Helmut-Schmidt-Univesität, Universität der Bundeswehr Hamburg, Hamburg, Germany, 2018. (In German)

17. Schaffarczyk, A.; Boisard, R.; Boorsma, K.; Dose, B.; Lienard, C.; Madsen, T.L.H.Å.; Rahimi, H.; Reichstein, T.; Schepers, G.; Sørensen, N.; et al. Comparison od 3D transitional CFD simulations for rotating wings with measurements. *J. Phys. Conf. Ser.* **2018**. [CrossRef]
18. Troen, I.; Lundtang Petersen, E. *European Wind Atlas*; Technical Report; Risø National Laboratory: Rosklilde, Denmark, 1989.
19. Schaffarczyk, A.P.; Schwab, D.; Ingwersen, S.; Breuer, M. Pressure and hot-film measurements on a wind turbine blade operating in the atmosphere. *J. Phys. Conf. Ser.* **2014**, *555*, 012092. [CrossRef]
20. de Luca, L.; Carlomagno, G.M.; Buresti, G. Boundary layer diagnostics by means of an infrared scanning radiometer. *Exp. Fluids* **1990**, *9*, 121–128. [CrossRef]
21. Gartenberg, E.; Roberts, A.S. Airfoil transition and separation studies using an infrared imaging system. *J. Aircraft* **1991**, *28*, 225–230. [CrossRef]
22. Dollinger, C.; Sorg, M.; Balaresque, N.; Fischer, A. Measurement uncertainty of IR thermographic flow visualization measurements for transition detection on wind turbines in operation. *Exp. Ther. Fluid Sci.* **2018**, *97*, 279–289. [CrossRef]
23. Wolf, C.C.; Mertens, C.; Gardner, A.D.; Dollinger, C.; Fischer, A. Optimization of differential infrared thermography for unsteady boundary layer transition measurement. *Exp. Fluids* **2019**, *60*. [CrossRef]
24. Dollinger, C.; Balaresque, N.; Sorg, M.; Fischer, A. IR thermographic visualization of flow separation in applications with low thermal contrast. *Infrared Phys. Technol.* **2018**, *88*, 254–264. [CrossRef]
25. Gartenberg, E.; Roberts, A.S. Twenty-five years of aerodynamic research with infrared imaging. *J. Aircraft* **1992**, *29*, 161–171. [CrossRef]
26. Joseph, L.A.; Borgoltz, A.; Devenport, W. Infrared thermography for detection of laminar-turbulent transition in low-speed wind tunnel testing. *Exp. Fluids* **2016**, *57*, 77. [CrossRef]
27. Montelpare, S.; Ricci, R. A thermographic method to evaluate the local boundary layer separation phenomena on aerodynamic bodies operating at low Reynolds number. *Int. J. Therm. Sci.* **2004**, *43*, 315–329. [CrossRef]
28. Crawford, B.K.; Duncan, G.T.; West, D.E.; Saric, W.S. Robust, automated processing of IR thermography for quantitative boundary-layer transition measurements. *Exp. Fluids* **2015**, *56*, 149. [CrossRef]
29. Richter, K.; Schülein, E. Boundary-layer transition measurements on hovering helicopter rotors by infrared thermography. *Exp. Fluids* **2014**, *55*, 1755. [CrossRef]
30. Dollinger, C.; Balaresque, N.; Gaudern, N.; Gleichauf, D.; Sorg, M.; Fischer, A. IR thermographic flow visualization for the quantification of boundary layer flow disturbances due to the leading edge condition. *Renew. Energy* **2019**, *138*, 709–721. [CrossRef]
31. XFOIL v6.99. Available online: https://web.mit.edu/drela/Public/web/xfoil/ (accessed on 21 March 2019).
32. *Installation and User Manual of the FLOWer Main Version, Release 1-2008.1*; Technical Report; Deutsches Zentrum für Luft- und Raumfahrt e.V., Institute of Aerodynamics and Flow Technology: Göttingen, Germany, 2008.
33. Mack, L.M. *Transition and Laminar Instability*; Technical Report NASA-CP-153203; JPL-PUBL-77-15; Jet Propulsion Laboratory, California Institute of Technology: Pasadena, CA, USA, 1977.
34. Mack, L.M. *Boundary-Layer Linear Stability Theory*; Technical Report 709; AGARD: Neuilly-sur-Seine, France, 1984.
35. Schülein, E. Experimental Investigation of Laminar Flow Control on a Supersonic Swept Wing by Suction. In Proceedings of the AIAA-2008-4208, 4th Flow Control Conference, Seattle, WA, USA, 23–26 June 2008.